Welding in the World (2024) 68:637–655
https://doi.org/10.1007/s40194-023-01661-w

RESEARCH PAPER

Low alloy steel girth welds in X65 steel pipes internally clad with alloy 625

Part I: Materials selection and process development

Alejandro Alvarez[1] · Martin Schmitz-Niederau[2] · Hermann-Josef Weber[2] · Boian T. Alexandrov[1]

Received: 8 August 2023 / Accepted: 7 December 2023 / Published online: 9 January 2024

Abstract
API 5L Grade X65 steel pipes, internally clad alloy 625, are commonly utilized in pipelines and risers for subsea oil and gas extraction. Gird welds in such pipes are conventionally made using alloy 625 filler metal. However, alloy 625 weld metal cannot meet the base metal yield strength overmatching requirement for subsea reel lay installation. This study explored materials selection and process development for low-alloy steel girth welds in API 5L Grade X65 steel pipes, internally clad with alloy 625. Welding with a higher melting point filler metal over a lower melting substrate, i.e., low-alloy steel over Ni-based alloy, is impractical due to increased susceptibility to solidification cracking and solidification shrinkage porosity. Pseudo-binary phase diagrams developed for various combinations of low alloy steel filler metals and Ni-based alloy substrates identified good compatibility between ER80S-G filler metal and alloy 686. The solidification temperature range and the tendency for partitioning of alloying elements were significantly lower throughout the entire ER80S-G/alloy 686 dilution range than in the low alloy steel filler metals/alloy 625 combinations. Extensive process optimization effort to reduce the dilution of alloy 686 root pass in the low-alloy steel weld metal and avoid incomplete fusion defects allowed for the production of defect-free girth welds. These welds met the yield strength and ductility requirements for subsea reel lay installation of pipelines. Process optimization for bead tempering significantly narrowed the high hardness region in the ER80S-G/alloy 686 partially mixed zone.

Keywords Material selection · Process development · Low-alloy steel and Ni-based welding filler metals · Internally clad X65 steel pipes · Girth welds

1 Introduction

API 5L Grade X65, X70, and X80 steels are commonly used for the manufacturing of oil and gas pipelines and risers [1]. To improve the resistance to transported corrosive fluids, such pipelines are internally clad with corrosion-resistant Ni-based alloys, such as alloy 625 [2]. Girth welding of internally clad pipes is of particular importance to the oil and gas industry. Not only do such girth welds influence manufacturing expenses, but they also determine the method of pipeline installation.

Reel lay is a method of subsea pipeline installation that helps reduce manufacturing expenses since welding, inspection, coating, and testing are all performed onshore [3]. After manufacturing is complete, pipelines are reeled into an offshore vessel and transported to a destination where they are unreeled, straightened, and installed. During the reeling and installation processes, pipelines may undergo local plastic deformation that could cause wall thinning and loss of strength in localized areas [3]. DNV has established manufacturing requirements to limit mechanical property degradation in reel lay applications [4]. According to these

Recommended for publication by Commission II - Arc Welding and Filler Metals

✉ Boian T. Alexandrov
alexandrov.1@osu.edu

[1] Department of Materials Science and Engineering, The Ohio State University, Columbus, OH, USA

[2] voestalpine Böhler Welding Germany GmbH, Hamm, Germany

requirements, girth welds shall overmatch the base metal yield strength by 100 MPa. Additional requirements include 250 HV_{10} maximum hardness in the girth weld metal and HAZ, passing ASME Section IX bend test, and Charpy impact energy greater than 38-J in the base metal, girth weld metal, and HAZ.

API 5L Grade X65 and X70 pipes internally clad with alloy 625 are currently joined using Alloy 625 filler metal girth welds. Alloy 625 weld metals, however, exhibit yield strengths in the order of 460 MPa, which may be acceptable for reel lay of lower-grade line pipe steels than X65. Achieving the 100 MPa weld metal yield strength overmatch for X65 pipes requires utilizing precipitation-strengthened Ni-based alloy, super-duplex stainless steel, and/or low alloy steel (LAS) filler metals. Utilizing LAS filler metals as a more cost-effective solution for welding internally clad pipes has been an ongoing challenge to the oil and gas industry. Welding with a higher solidus temperature LAS filler metal over a lower melting temperature Ni-based alloy clad layer results in high dilution and partitioning of alloying elements, leading to increased susceptibility to solidification cracking and the formation of shrinkage porosity, brittle intermetallics, and microstructural constituents [5] [6].

A practical solution for joining internally clad X65 line pipes with LAS girth welds, which avoids welding with LAS filler metal over Alloy 625 substrate, has been successfully developed and qualified [7, 8]. The welding procedure consists of a 3-step process to fill a U-groove girth weld. Step 1 involves a partial penetration LAS root pass and hot pass on the external side of the U-groove performed with a gas metal arc pulse (GMAWp) process. Step 2 utilizes automated gas tungsten arc welding (GTAW) with alloy 625 filler metal on the internal side of the U-groove root. In step 3, the girth weld is completed on the U-groove external side using the GMAWp process with the LAS filler metal. This procedure has been tested and proven to comply with DNV requirements for reel-lay installation of pipelines. However, its application is limited to shorter- and/or bigger-diameter pipes that provide direct access to the U-groove internal side.

The objective of this study was the development of a narrow groove GMA process that enables wielding with LAS filler metals over a Ni-based root pass in girth welds of internally clad API Grade X65 pipes. The research focused on filler metal selection and process development, optimization, and validation, aiming to produce defect-free welds that meet the DNV requirements for reel lay applications.

2 Materials and procedure

2.1 Materials

The chemical compositions of the base and filler metals used in this study are presented in Table 1. Plates of API 5L Grade X65 steel were welded in narrow U-groove configurations, as shown in Fig. 1. The girth weld fill passes were performed

Table 1 Materials chemical composition

Material	Chemical composition (wt. %)											
	C	Cr	Mo	Mn	Ni	Si	V	W	N	Nb	Ti	Fe
Filler metal												
ER80S-G	0.062	0.024	0.003	1.54	0.85	0.656	0.0003	0.007	0.004	0.003	0.066	Bal.
ER100S-G	0.108	0.278	0.478	1.62	0.926	0.57	0.001	0.004		0.003	0.003	Bal.
FM-686	0.006	21.3	15.6	0.272	59.0	0.032	0.005	3.1		0.013	0.09	0.161
FM-625	0.011	21.6	8.7	0.021	65.3	0.1	0.005	0.007	0.012	3.425	0.173	0.457
API 5L Grade X65	0.096	0.3	0.12	1.41	0.12	0.24	0.028		0.0084	0.03	0.012	Bal.

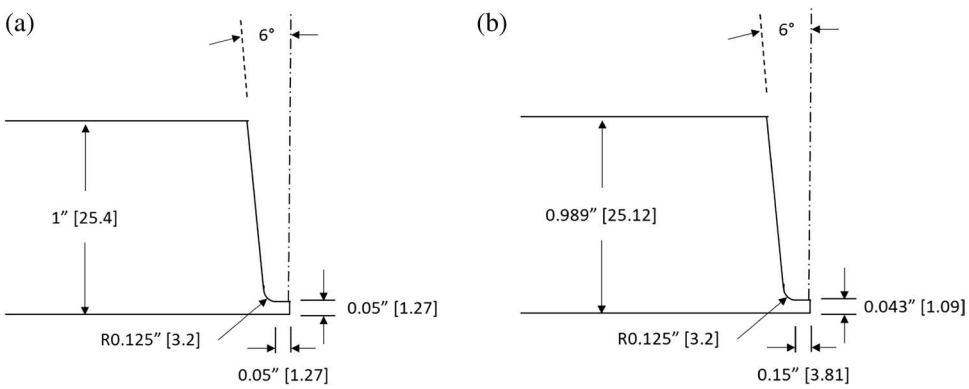

Fig. 1 Narrow U-groove designs: (a) in welds 1 through 6 and (b) in welds 7, 8, and 9

using low-alloy filler metals AWS A5.28 ER100S-G and ER80S-G [9]. Ni-based filler metals AWS A.5.14 ERNiCrMo-14 (FM-686) and ERNiCrMo-3 (FM-625) [10] were considered for the girth welds root pass.

2.2 Thermodynamic simulations

Thermodynamic simulations with ThermoCalc™ were performed to analyze the solidification behavior of the dissimilar transition zones between the LAS filler metals and the Ni-based root passes and screen their compatibility. The pseudo-binary phase diagrams in Figs. 2 and 3 were developed by performing Scheil–Gulliver solidification simulations in 1% dilution increments, ranging from undiluted LAS filler metal to undilute Ni-based root pass. The TCFE10 and TCNI9 databases were utilized for dilutions with prevailing iron and nickel content, respectively. Carbon was designated as a fast-diffusing element, and only the liquid, BCC, and FCC phases were considered in the simulations. Silicon and phosphorus were omitted from the analyses due to their tendency to underestimate predicted solidus temperatures. Based on previous research [11], the solidus temperature was determined to reach 0.98 for the solid fraction. The solidification temperature ranges of undiluted tested materials and of 50% LAS filler metal/NI-based alloy dilutions are summarized in Table 2.

The segregation behavior of carbon and the strong carbide formers, Mo and Nb in FM-625 and Mo and W in FM-686, was evaluated in relation to their effect on increasing solidification cracking susceptibility by forming eutectic

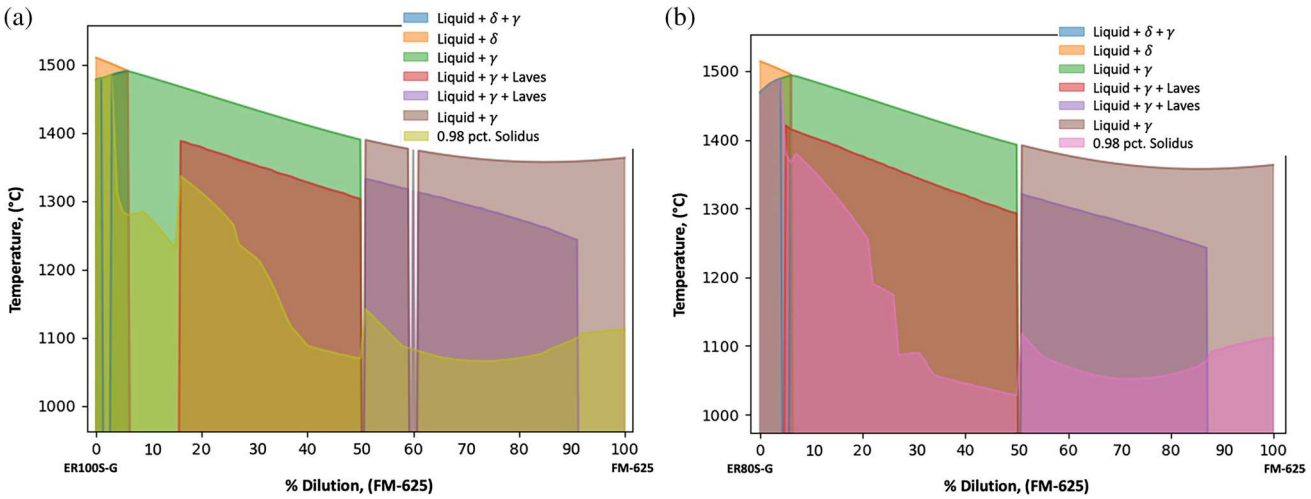

Fig. 2 Pseudo-binary solidification diagrams in weld metals of ER100S-G (**a**) and ER80S-G (**b**) diluted with FM-625

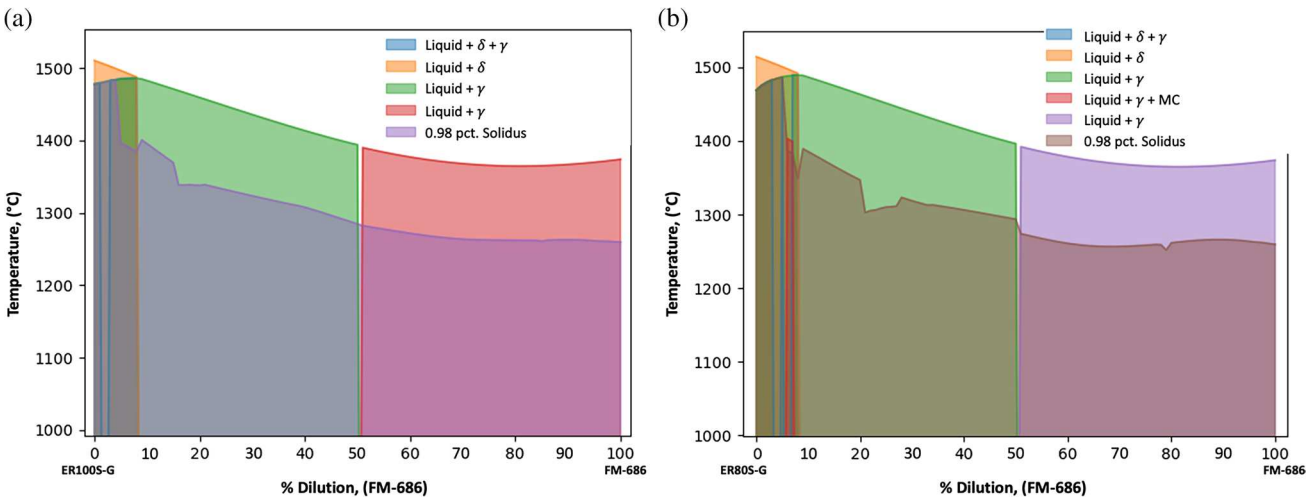

Fig. 3 Pseudo-binary solidification diagrams in weld metals of ER100S-G (**a**) and ER80S-G (**b**) diluted with FM-686

Table 2 ThermoCalc™-predicted solidification temperature ranges in the tested materials

Material	Liquidus (°C)	0.98 Solidus (°C)	STR (°C)
ER80S-G	1514	1411	103
ER100S-G	1510	1423	87
FM-686	1374	1264	110
FM-625	1362	1135	227
50% dilution	TCNI9: Fe-dependent element		
80S-686	1392	1282	110
80S-625	1384	1090	294
100S-686	1390	1285	105
100S-625	1386	1106	280
50% dilution	TCNI9: Ni-dependent element		
80S-686	1394	1288	106
80S-625	1393	1184	209
100S-686	1391	1301	91
100S-625	1391	1199	193

constituents. The partitioning coefficients of these elements were calculated near the terminal stages of solidification using Eq. (1) (Fig. 4a, b).

$$k = \frac{C_S}{C_L} \tag{1}$$

Where k is the partitioning coefficient, C_S is the element content in the solid at the solid/liquid interface, and C_L is the element content in the liquid at the solid/liquid interface.

Simulations of non-equilibrium cooling were performed to compare predicted volume fractions of BCC, FCC, martensite, and Laves phase in ER100S-G and ER80S-G welds diluted with FM-686 root pass. Property diagrams were first developed using ThermoCalc™ to determine the volume fraction of BCC present at room temperature. The remaining fraction was assumed to be a mixture of FCC and martensite. A single-point equilibrium calculation was performed at the A_3 temperature to determine the volume fraction of austenite. The chemical composition of FCC at A_3 was used with ThermoCalc™ to predict the FCC fraction that would decompose to martensite upon cooling. Simulations were repeated at 10% dilution intervals with additional calculations at 15 and 25% dilution, as shown in Fig. 5.

2.3 Welding process development

Welding trials were carried out using a Yaskawa Motoman MA1400 six-axis robotic arm with a Fronius CMT Advanced power supply equipped with an RCU 5000i user interface. The weld root and backing passes were deposited using gas metal arc pulse (GMAW-P) and cold metal transfer (CMT) processes with 1.0 mm diameter FM-686 filler metal in shielding gas mixture Ar/30%He/0.5%CO_2. The weld fill passes were deposited with various combinations of CMT, short-circuit (GMAW-SC), spray (GMAW-S), and GMAW-P processes, using 1.2 mm ER100S-G or 1.0 mm EG80S-G filler metals in shielding gas mixture 85%Ar/15%CO_2.

The welding trials were performed in the groove geometries shown in Fig. 1. The steel plates were restrained to the work table by tack welding and clamped to minimize distortion. Preheat and interpass temperatures were maintained between 100 and 125°C and controlled with a type K thermocouple. The process development trials involved nine groove welds, utilizing one-, two-, and three-pass per-layer procedures shown in Fig. 6. The sets of welding parameters for the nine groove welds are displayed in Tables 3, 4, 5, and 6. The groove configuration shown in Fig. 1a was utilized for welds 1 through 6 and the groove in Fig. 1b for welds 7, 8, and 9.

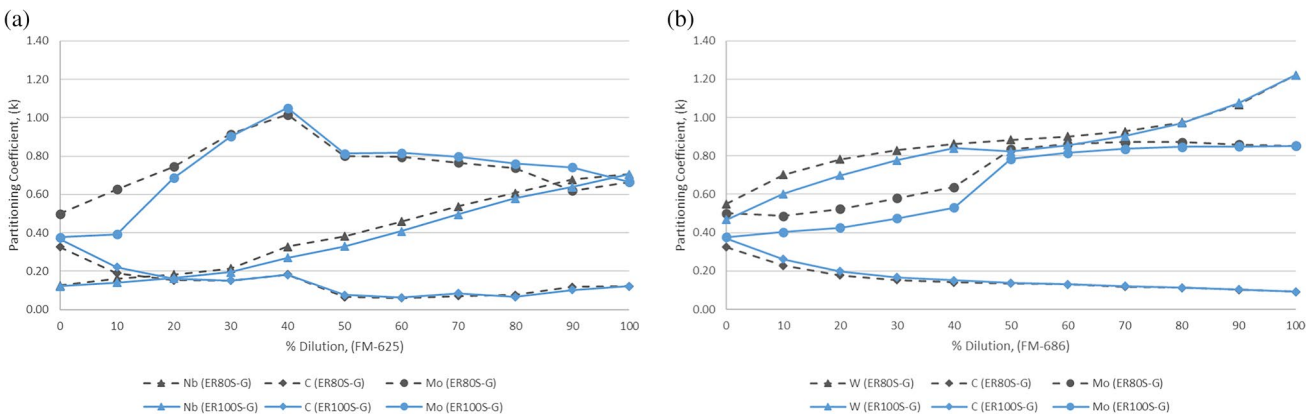

Fig. 4 Partitioning coefficients (k) for weld metals of ER100S-G (**a**) and ER80S-G (**b**) diluted with FM-686

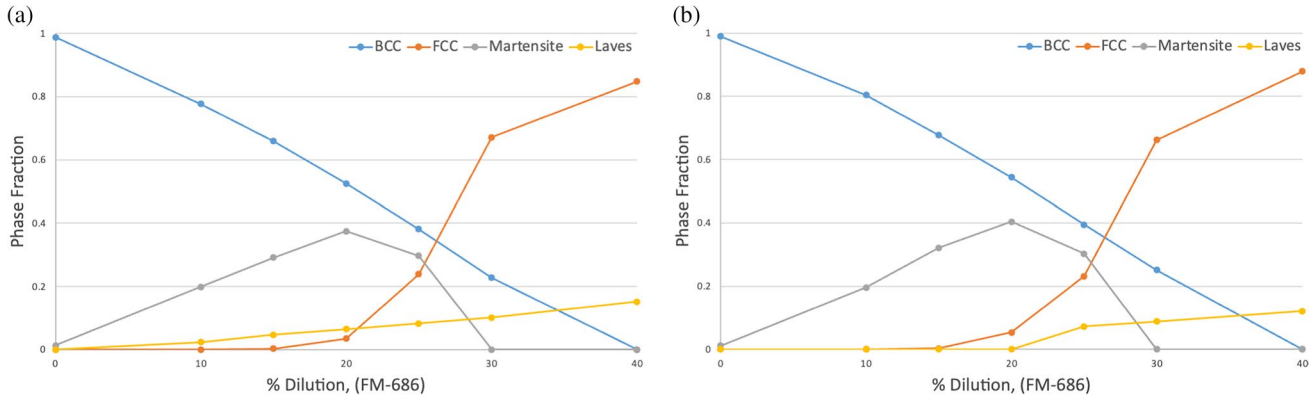

Fig. 5 Predicted content of microstructural constituents in weld metals of ER100S-G (**a**) and ER80S-G (**b**) diluted with FM-686

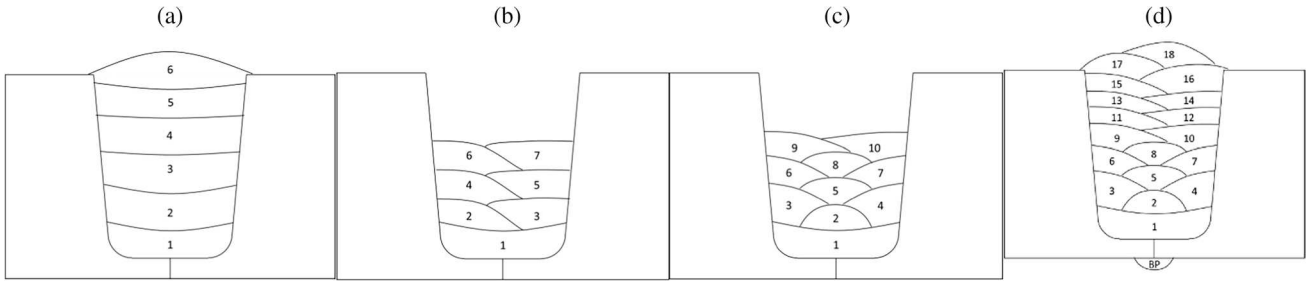

Fig. 6 Weld bead schematics: **a** welds 1, 2, and 3; **b** weld 4; **c** weld 5; and **d** welds 6 through 9. Groove design: narrow gap (Fig. 1a) for welds 1 through 6; wide gap (Fig. 1b) for welds 7, 8, and 9. Root pass: FM-686. Fill passes: ER100S-G for welds 1, 2, and 3; ER80S-G for welds 4 through 9

2.4 Metallurgical characterization

Each weldment was cross-sectioned, mounted, and polished using standard metallographic procedures. Etching consisted of a two-step process to reveal the microstructure of both the low-alloy steel base and filler metals and the Ni-based root pass. Etching in 2% Nital solution for 10 s was followed by electrolytic etching with 10% chromic acid (3 volts, 0.25 amps) for 3 s. Etched samples were analyzed using an Olympus GX51 light microscope.

2.5 Mechanical testing

Specimen extraction and mechanical testing were performed in accordance with DNV-OS-F101 [4]. Transverse weld metal tensile specimens, as shown in Fig. 7, were extracted 1 in. away from the weld start and finish. Tensile testing was conducted using the 810 MTS test frame in accordance with ASTM E8. Based on the gauge section length and the Grade X65 steel yield strength, the displacement rate for the entirety of the test was set to 0.014 in./min.

Bend testing was conducted according to DNV-OS-F101 and ASME BPVC Section IX, utilizing a pneumatic guided-bend roller jig. Side bend specimens were extracted across the middle of the groove weld. Specimens were 10 mm thick, 19.05 mm wide, and 200 mm long. The weld cap and root reinforcements were machined flat, and a radius of 3 mm was machined to all sample edges. Dimensions for the guided-bend roller jig were determined by ASME Section IX to apply 20% strain to the bend test specimen. After testing, each specimen was analyzed and inspected for defects and/or discontinuities.

Hardness testing was performed using a Leco LM 100AT Vickers Microhardness Tester with a 300-g load, and indent spacing of 250–300 µm. Hardness maps were designed to cover most of the welded area.

3 Results

3.1 Solidification behavior predictions

The pseudo-binary phase diagrams in Figs. 2 and 3 show significant differences in the solidification behavior of ER100S-G and ER80S-G weld metals diluted with FM-625 and FM-686 root passes. Dilution below 5 to 8% with both

Table 3 Welding parameters for welds 1, 2, and 3: single-pass per-layer trial

Weld No./figure	Bead sequence/groove	Filler metal	Synergic line	Welding process	Pass No.	Weave amplitude (mm)	Weave frequency (Hz)	Dwell time (s)	Wire feed speed (mm/s)	Travel speed (mm/s)	WFS/TS
1/8a, 9a	1-pass per layer/narrow gap	FM-686	888	GMAW-P	1	1.3	4.7	0.1	143.9	8.5	16.9
		ER100S-G	1360	CMT	2	2.65	2	0.1	122.8	4.2	29.2
					3	2.95					
					4	3.35					
					5	3.65					
					6	3.85					
2/8b	1-pass per layer/narrow gap	FM-686	888	GMAW-P	1	1.3	4.7	0.1	143.9	8.5	16.9
		ER100S-G	1362	GMAW-S	2	2.2	3.7	0.1	118.5	3.0	39.5
					3–4	2.4			135.5	3.8	35.7
					5	2.5					
					6	2.6					
3/8c, 9b	1-pass per layer/narrow gap	FM-686	888	GMAW-P	1	1.3	4.7	0.1	143.9	8.5	16.9
		ER100S-G	1362	GMAW-S	2	2.35	3.7	0.1	135.5	3.8	35.7
					3–4	2.4					
					5	2.5					
					6	2.6					

Table 4 Welding parameters for welds 3, 4, and 5: bead tempering trial

Weld No./figure	Bead sequence/groove	Filler metal	Synergic line	Welding process	Pass No.	Weave amplitude (mm)	Weave frequency (Hz)	Dwell time (s)	Wire feed speed (mm/s)	Travel speed (mm/s)	WFS/TS
3/8c, 9b	1-pass per layer/narrow gap	FM-686	888	GMAW-P	1	1.3	4.7	0.1	143.9	8.5	16.9
		ER100S-G	1362	GMAW-S	2	2.35	3.7	0.1	135.5	3.8	35.7
					3–4	2.4					
					5	2.5					
					6	2.6					
4/9c	2-passes per layer/narrow gap	FM-686	888	GMAW-P	1	1.2	4.2	0.1	141.8	7.2	19.7
		ER80S-G	1360	CMT	2	0.8	5	0.1	88.9	8.0	11.1
					3				91.0		11.4
					4	0.9			97.4	8.5	11.5
					5				101.6		12.0
					6–7	1					12.0
5/9d, 10a	3-passes per layer/narrow gap	FM-686	888	GMAW-P	1	1	4.2	0.1	118.5	6.8	17.4
		ER80S-G	1360	CMT	2	0.2	5	0.1	120.7	9.3	13.0
					3–4				127.0	6.8	18.7
					5					8.0	15.9
					6–7	0.4				6.8	18.7
					8	0.3				8.0	15.9
					9–10	0.8				6.8	18.7

Table 5 Welding parameters for welds 6 and 7: avoiding incomplete fusion defects trial

Weld No./figure	Bead sequence/groove	Filler metal	Synergic line	Welding process	Pass No.	Weave amplitude (mm)	Weave frequency (Hz)	Dwell time (s)	Wire feed speed (mm/s)	Travel speed (mm/s)	WFS/TS
6/10b	3-passes per layer/narrow gap	FM-686	1254	CMT	BP	0	0	0	55.0	4.7	11.7
			888	GMAW-P	1	1.2	3	0.1	118.5	5.5	21.5
		ER80S-G	1360	CMT	2	1.2	4.5	0.1	42.3	8.5	5.0
			124	GMAW-SC	3–4	0	0	0	78.3	6.8	11.5
					5	1	4.5	0.1		8.0	9.8
					6–7	0	0	0		6.8	11.5
					8	1	4.5	0.1		8.0	9.8
			1156	GMAW-P	9–18	0.8	0		173.6	11.4	15.2
7/10c, 11a	3-passes per layer/wider gap	FM-686	1254	CMT	BP	0	0	0	55.0	4.7	11.7
			888	GMAW-P	1	3.5	3.1	0.1	137.6	6.4	21.5
		ER80S-G	1360	CMT	2	1.2	4.5	0.1	42.3	8.5	5.0
			124	GMAW-SC	3–4	1.6	2.5	0	88.9	4.7	18.9
					5	1.2	4.5	0.1	78.3	8.0	9.8
					6–7	1.5	2.5	0	88.9	4.7	18.9
					8	1.2	4.5	0.1	78.3	8.0	9.8
			1156	GMAW-P	9–10	1.4	4		173.6	10.6	16.4
					11–16	1.5					
					17–18	1.6					

Table 6 Welding parameters for welds 8 and 9: final optimization trial

Weld No./figure	Bead sequence/groove	Filler metal	Synergic line	Welding process	Pass No.	Weave amplitude (mm)	Weave frequency (Hz)	Dwell time (s)	Wire feed speed (mm/s)	Travel speed (mm/s)	WFS/TS
8/11b	3-passes per layer/wider gap	FM-686	1254	CMT	BP	0	0	0	55.0	4.7	11.7
			888	GMAW-P	1	3.5	3.1	0.1	141.8	6.4	22.2
		ER80S-G	1360	CMT	2	1.2	4.5	0.1	42.3	8.5	5.0
			1156	GMAW-P	3–4	1.4	3	0	173.6	11.9	14.6
			124	GMAW-SC	5	1.2	4.5	0.1	78.3	8.0	9.8
			1156	GMAW-P	6–7	1.4	3	0	173.6	11.9	14.6
			124	GMAW-SC	8	1.2	4.5	0.1	78.3	8.0	9.8
			1156	GMAW-P	9	1.4	4		173.6	10.6	16.4
					10–16	1.5					
					17–18	1.6					
9/11c	3-passes per layer/wider gap	FM-686	1254	CMT	BP	0	0	0	55.0	4.7	11.7
			888	GMAW-P	1	3.5	3.1	0.1	141.8	6.4	22.2
		ER80S-G	1156	GMAW-P	2	0	0	0	173.6	12.7	13.7
					3–4	1.4	3			11.9	14.6
					5	0	0			12.7	13.7
					6–7	1.4	3			11.9	14.6
					8	0	0			12.7	13.7
					9–10	1.4	4	0.1		10.6	16.4
					11–15	1.5					
					16–18	1.6					

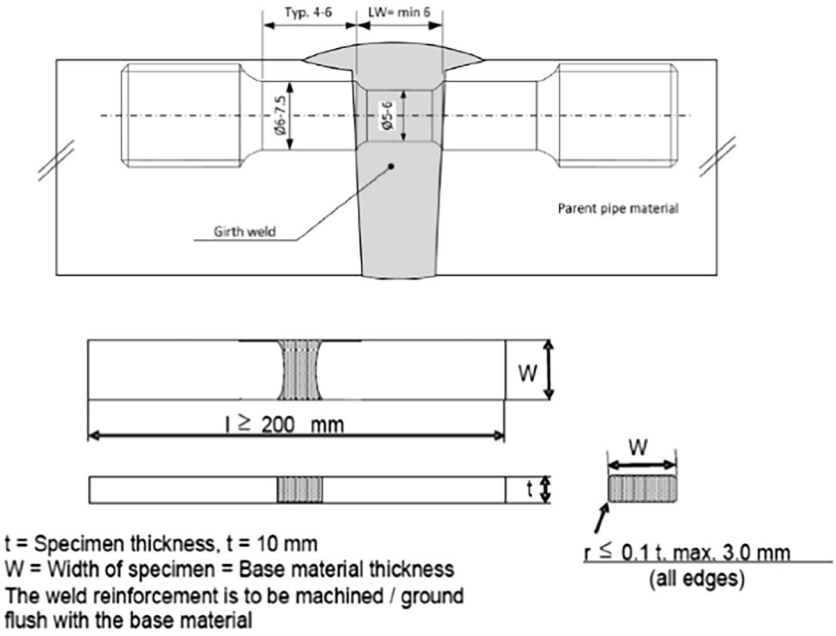

Fig. 7 Cross-weld tensile test and bend test specimens in accordance with DNV-OS-F101

root passes results in δ-phase solidification. Dilution with more than 5% FM-625 root pass results in γ-phase solidification, which is followed by the formation of Laves phase (Fig. 2). Laves phase is predicted to form between 15 and 92% dilution for ER100S-G and between 5 and 87% dilution for ER80S-G, covering most of the solidification temperature ranges (STRs). Maximum STRs of 280 and 294°C, respectively, for filler metals ER100S-G and ER80S-G, are predicted at 50% dilution with FM-625. Dilution with more than 8% FM-686 root pass in both LAS filler metals leads to γ-phase solidification with STRs of about 90 to 110°C (Fig. 3).

The partitioning coefficients of carbon and the alloying elements with the strongest tendency for segregation during solidification in both LAS weld metals diluted with FM-625 and FM-686 root passes are shown in Fig. 4. The LAS weld metals have an insignificant effect on the partitioning of C, Mo, Nb, and W. Carbon partitions strongly, showing partitioning coefficient (k) values below 0.2 with both substrates. Dilution from FM-625 results in strong partitioning of Nb, with k values below 0.2 between 10 and 30% dilution, and in moderate partitioning of Mo (Fig. 4a). Dilution from FM-686 results in stronger partitioning of Mo, with k values below 0.5 between 10 and 40% dilution and moderate partitioning of W below 80% dilution.

3.2 Microstructure predictions

The microstructure in ER100S-G and ER80S-G weld metals was predicted by analyzing equilibrium and meta-stable phase transformations using ThermoCalc™. Fig. 5 shows that dilution with up to 40% FM-686 has a similar effect on the content of microstructural constituents in both weld metals. The BCC phase, which can include ferrite and various forms of bainite, is predicted to be present up to 40% dilution. Dilutions above 15% lead to the retention of austenite, which becomes the dominant weld metal constituent above 30% dilution. Martensite is predicted to form up to a 30% dilution with a maximum of 0.4-phase fraction at 20% dilution. Up to 0.18 phase fraction of Laves phase is predicted to form in both weld metals, showing a slightly larger content in the RE100S-G weld metal. This prediction is questionable due to the low Nb content in Alloy 686 and would need phase identification through metallurgical characterization.

3.3 Welding process development

The welding procedure and parameter development trials aimed at avoiding weld defects, minimizing FM-686 root pass dilution in the weld metal, and reducing weld metal hardness. The first set of welding trials was focused on producing defect-free welds, utilizing the one-pass per layer procedure and parameters shown in Fig. 6a and Table 2. Cross sections of the resulting welds showed incoplete fusion defects (IFDs) and shrinkage porosity in welds 1 and 2, solidification cracking in weld 2, and a defect-free weld 3 (Fig. 8). The welds in this trial exhibited high dilution with the FM-686 root pass in layers 2 and 3 and hardness values exceeding 400 $HV_{0.3}$, with bead tempering effects in the subsequent layers (Fig. 9a, b).

The following optimization step, summarized in Table 4, aimed at reducing dilution with the FM-686 root pass and promoting bead tempering. Moving to two beads per layer in weld 4 resulted in some tempering in layer 3, but layer 2

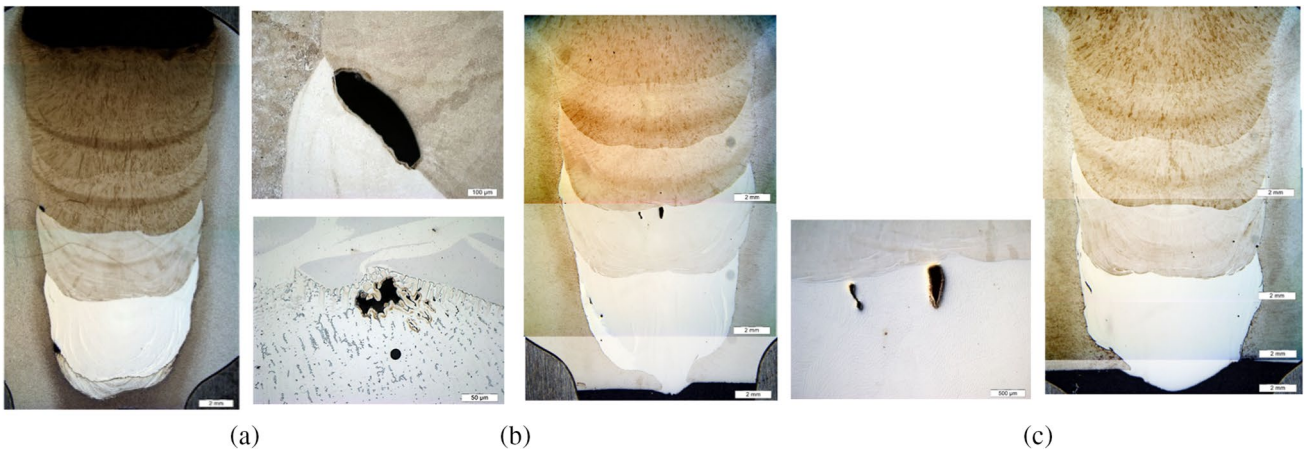

Fig. 8 Cross sections of single bead per pass welds: **a** weld 1 CMT fill passes, incomplete fusion defects, and shrinkage porosity; **b** weld 2 GMAW-S fill passes, center-line solidification cracking, and shrinkage porosity, weld 3 GMAW-S fill passes, no defects. Welding parameters are in shown Table 3

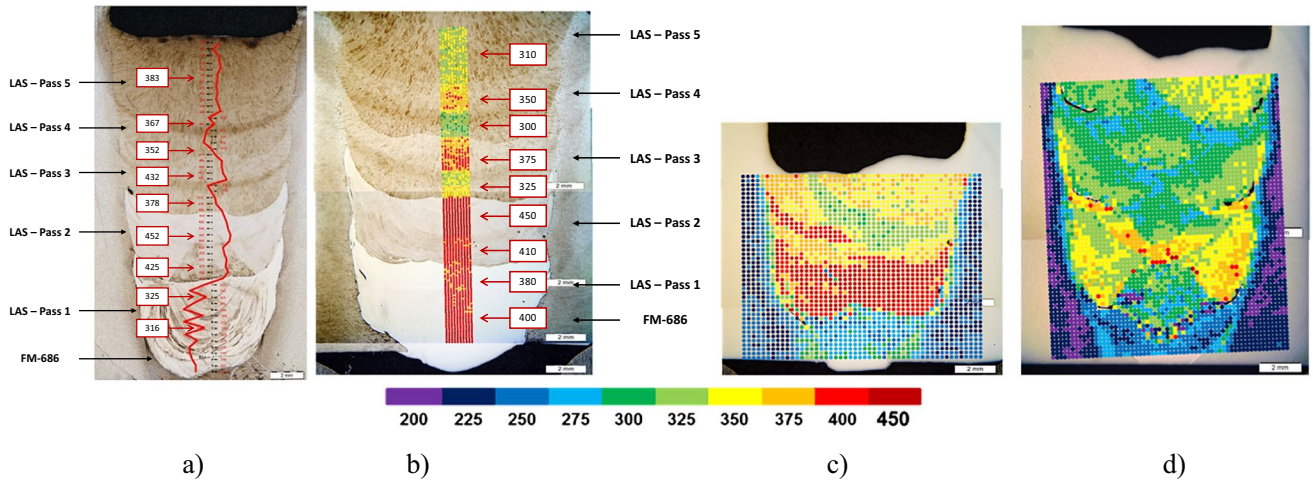

Fig. 9 Effect of bead sequence on hardness ($HV_{0.3}$): **a** weld 1 and **b** weld 3—single pass per layer; **c** weld 4—two passes per layer; and **d** weld 5—three passes per layer. Welds 1, 4, and 5—CMT fill passes; weld 3—GMAW-S fill passes. Filler metals: ER100S-G in welds 1 and 3, ER80S-G in welds 4 and 5. Welding parameters are shown in Table 4

was still in the hardness range of 400 $HV_{0.3}$ (Fig. 9c). Using 3 beads per layer in weld 5 provided a significant bead tempering effect but generated multiple IFDs (Figs. 9d and 10a).

The third optimization step (Table 5) was developed to resolve the IFDs associated with the CMT process. Using GMAW-SC in combination with a wider groove geometry (Fig. 1b), we eliminated IFDs between the fill passes and the base metal, as shown in Fig. 10b, c. However, IFDs were still found between fill passes (Fig. 10c). Utilizing the GMAW-P process in the final optimization step (Table 6; Fig. 11), we eliminated the interpass IFDs. Using GMAW-SC for the central passes in layers 3 and 4 of weld 8 reduced dilution with FM-686 and provided favorable hardness distribution (Fig. 11b).

3.4 Mechanical properties

Weld 7 was subjected to tensile and bend testing in accordance with DNV-OS-F101. Cross-weld tensile specimens were extracted from the weld central zone and at 25 mm from the weld start and stop locations. Three cross-weld bend specimens were extracted from the central zone. As shown in Table 7, all tensile test specimens satisfied the DNV-OS-F101 requirement for overmatching the base metal yield strength by 100 MPa.

Two of the three bending specimens were free of open defects and met DNV-OS-F101 and ASME Section IX bend testing requirements (Fig. 12a, b). However, the third specimen contained a crack larger than the 3 mm

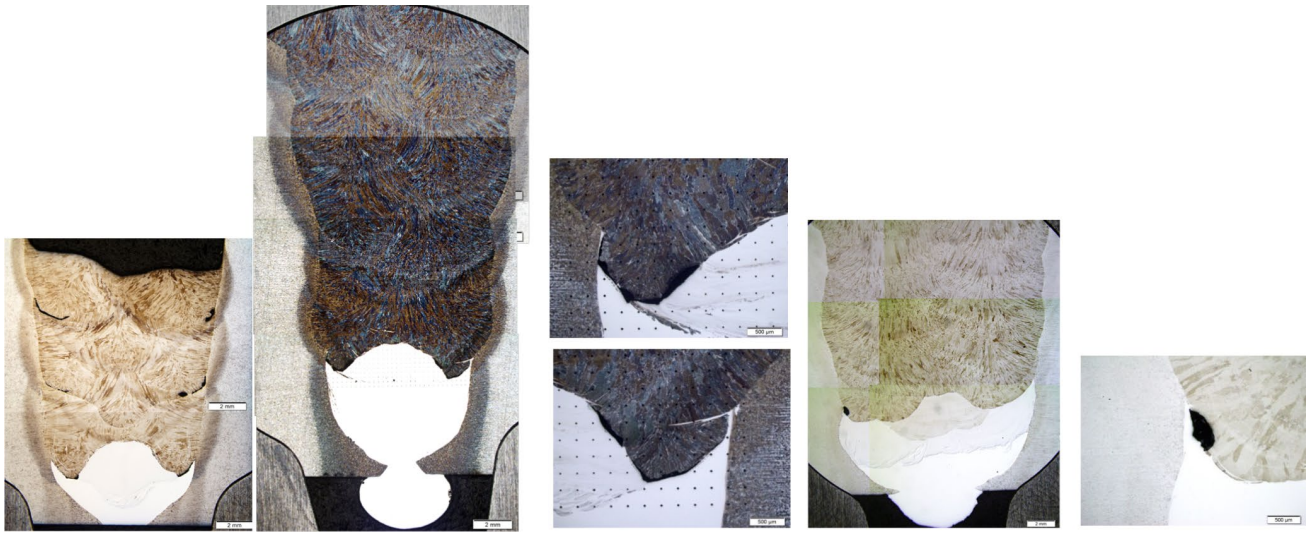

Fig. 10. Effect of welding process and groove geometry on the formation of incomplete fusion defects. Three pass-per-layer procedures. **a** Weld 5—CMT fill passes; **b** weld 6 and **c** weld 7—GMAW-SC fill passes. Welds 5 and 6—narrow gap grooves. Weld 7–wide gap groove. Welding parameters are shown in Tables 4 and 5

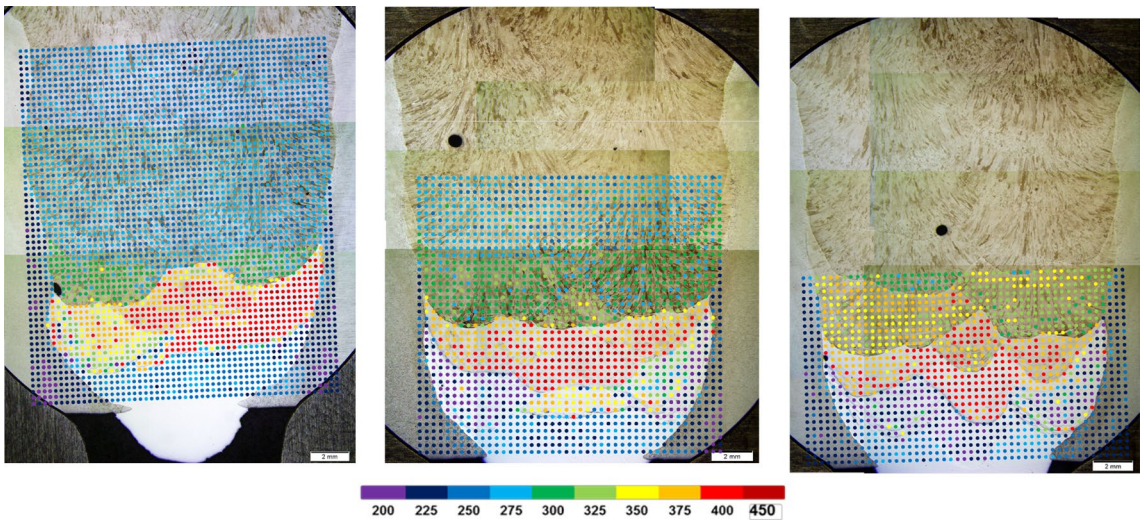

Fig. 11 Process optimization for bead tempering. Fill passes: Weld 7 – GMAW-SC, Weld 8 – GMAW-P and GMAW-SC, Weld 9 -GMAW-P. Welding parameters are shown in Tables 5 and 6

Table 7 Tensile test results from weld 7

Specimen extraction	YS (MPa)	UTS (MPa)	El. (%)
25 mm from weld start	624	683	13
Weld center	710	773	14
25 mm from weld stop	716	778	14

limit, which appeared to have originated from an incomplete fusion defect similar to the one observed in Fig. 10c. None of the three bend samples exhibited disbonding between layers of the ER80S-G/FM-686 dissimilar metal weld.

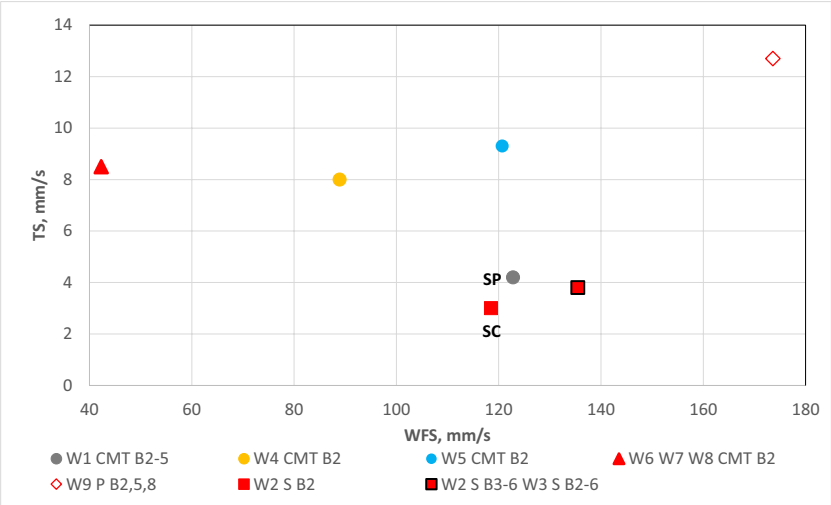

Fig. 12 Effect of WFS and TS of fill pass B2 on shrinkage porosity (SP) and solidification crack (SC) formation. Welds W1 through W9, processes: CMT, GMAW-P, and GMAW-S

4 Discussion

4.1 Filler metal selection

The objective of this study was to identify the combination of LAS filler metals and corrosion-resistant Ni-based alloy root passes that can produce resistance to hot cracking of dissimilar metal welds. Such a combination of higher STR filler metals with lower STR substrates typically results in solidification cracking, liquation cracking, and/or shrinkage porosity in the dissimilar transition zone [5] [6]. This is due to the formation of two opposite solidification fronts, originating off the higher STR LAS filler metal and off the lower STR Ni-based substrate, meeting in the dissimilar transition zone. The ER100S-G and ER80S-G filler metals considered in this study have narrow STRs of 103 and 87°C, respectively, with solidus temperatures of about 60°C above the liquidus and 280°C above the solidus temperatures of FM-625 (Fig. 2; Table 2). Dilution of FM-625 in the LAS filler metals extends the dissimilar metal welds STR up to 294°C due to the formation of the Nb-rich Laves phase. Iron is known to cause partitioning of Nb to the liquid during solidification [12], and the Laves phase is related to increased solidification cracking susceptibility in Ni-based alloys [13]. Fig. 4 shows extensive partitioning of Nb and carbon in the dilution range of Laves phase formation. The thermodynamic simulations with ThermoCalc™ demonstrated conditions for high susceptibility to hot cracking in DMWs of LAS filler metals over FM-625 root pass, including wide STR, formation of Laves phase, and potential for opposite solidification fronts throughout most of the dilution range. Susceptibility to solidification cracking and shrinkage porosity in similar DMWs was experimentally demonstrated in previous research [5].

The SRTs in weld metals of ER100S-G and ER80S-G diluted with FM-686 root pass are considerably narrower, between 90 and 110°C, without Laves phase formation due to the insignificant Nb content (Fig. 4; Table 1). Moderate segregation of Mo at dilutions up to 40% (Fig. 5) did not affect the STR. The predicted solidus temperatures of the LAS filler metals are about 50°C above the liquidus and 160°C above the solidus temperatures of FM-686 (Fig. 3; Table 2). These temperature differences are smaller than in the LAS/FM-625 weld metals, showing lower potential for opposite-front solidification. The solidification behavior simulations identified FM-686 as less susceptible to solidification cracking and the formation of shrinkage than FM-625. FM-686 was selected for the root pass in the girth welds of API 5L Grade X65 internally clad pipes.

Both LAS filler metals exhibited similar solidification behavior when diluted with FM-625 and FM-686 substrates (Figs. 2 and 3). ER80S-G welds had a slightly lower tendency for partitioning of Nb and Mo in dilutions with FM-625 and for partitioning of Mo and W in dilutions with FM-686, compared to ER100S-G welds (Fig. 4). Dilution with FM-686 had a similar effect on the predicted final microstructure in welds of both LAS filler metals (Fig. 5). The first pass of LAS filler metal over a root pass of FM-686 is expected to have a fully austenitic microstructure above 40% dilution. Laves phase was predicted to form in both weld metals, with slightly higher content in the ER100S-G weld related to its higher content of Mo. The Laves phase was predicted to form in the solid state and, therefore, was not considered relevant to the weld metal solidification behavior.

A significant amount of martensitic constituent is predicted to form between 10 and 28% dilution with the FM-686 root pass. Previous research has shown that dilution of low carbon steels with a similar composition as the tested LAS filler metals in the dissimilar transition zone of Ni-based weld metals resulted in the formation of martensitic constituents with hardness exceeding 400 $HV_{0.1}$ [14]. Diffusion

simulations with Dictra™, combined with metallurgical characterization, attributed the formation of hard martensite to significant carbon depletion in the steel base metal and carbon accumulation in the dissimilar transition zone [15]. The potential for the formation of hard martensite in the first LAS filler metal passes presented a concern in meeting the maximum hardness requirement of 250 HV, especially for the higher-carbon ER100S-G. However, both LAS filler metals were tested in the process development experiments due to the better probability of ER100S-G fulfilling the 100-MPa base metal overmatching requirement.

4.2 Welding process development and optimization

The process development and optimization efforts were focused on resolving the incomplete fusion defects, solidification shrinkage porosity and solidification cracking, and reducing the hardness in the LAS fill passes partially mixed with the FM-686 root pass. The optimization variables included the welding process, wire feeding speed (WFS), travel speed (TS), and arc weaving parameters. In the welding process analysis, the WFS/TS ratio was used as an indicator of the relative amount of filler metal deposited per unit weld length, which defines the weld pool volume. The WFS/TS ratio is also indicative of the weld heat input since the welding current in GMAW processes is directly proportional to the WFS.

4.2.1 Shrinkage porosity and solidification cracking

The WFS, TS, and WFS/TS used in depositing weld pass B2 in all test welds are mapped in Figs. 12 and 13. Shrinkage porosity was found along the fusion boundary between the FM-686 root pass and the ER100S-G pass B2 in the single-pass per-layer CMT weld W1 and GMAW-S weld W2 (Fig. 8a, b). The high deposition rate and heat input of pass B2 in these welds lead to almost complete remelting of the FM-686 root pass, forming a large, heavily diluted weld pool. This created conditions for solidification shrinkage porosity identified in [5]: large volume shrinkage and potential opposing solidification fronts of a partially melted lower solidus substrate (FM-686) and a higher solidus weld pool (pass B2). The shrinkage porosity was mitigated in welds W4 through W9 by increasing the number of passes per layer. This allowed us to double the TS and reduce more than twice the WFS/TS ratio, as shown in Figs. 12 and 13, resulting in smaller weld pools and lower dilutions with the FM-686 substrate.

The centerline solidification cracking in pass B3 of weld W2 can be related to remelting the heavily diluted B2. A slight reduction of the WFS/TS ratio of B2 was sufficient to produce crack-free weld W3. The results of this study allowed us to identify a process window for defect-free deposition of ER100S-G and ER80S-G over FM-686 substrate, defined by WFS between 40 and 180 mm/s, TS higher than 8 mm/s, and a WFS/TS ratio below 15 (Figs. 12 and 13).

4.2.2 Incomplete Fusion defects

The process parameters of the sidewall fill passes in all welds are mapped in Figs. 14 and 15. No Incomplete fusion defects formed in the single-pass-per-layer GMAW-S weld W2 and in the two-pass-per-layer CMT weld W4 (Figs. 8c and 9c). The high heat input spray arc, combined with sufficient weaving (Table 2), was able to completely fuse the groove side walls and underlying beads. Compared to the CMT W1, the significantly lower deposition rate and the two-pass per-layer procedure with weaving helped the CMT W4 avoid incomplete fusion defects. However, high dilution

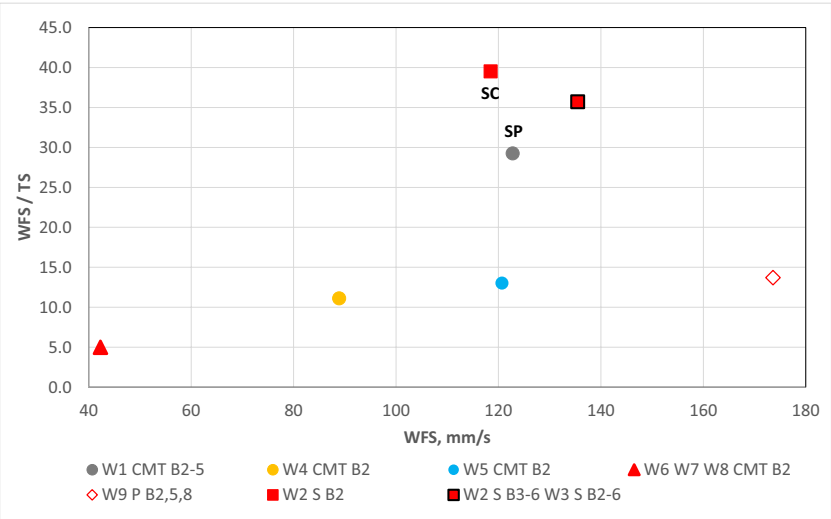

Fig. 13 Effect of WFS and WFS/TS of fill pass B2 on shrinkage porosity (SP) and solidification crack (SC) formation. Welds W1 through W9, processes: CMT, GMAW-P, and GMAW-S

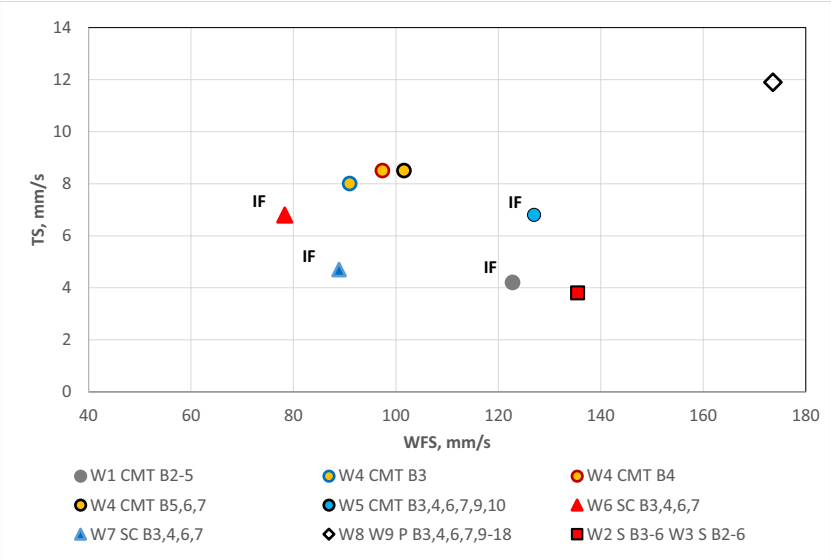

Fig. 14 Effect of WFS and TS of sidewall passes on incomplete fusion (IF) defects formation. Welds W1 through W9, processes: CMT, GMAW-SC, GMAW-P, and GMAW-S

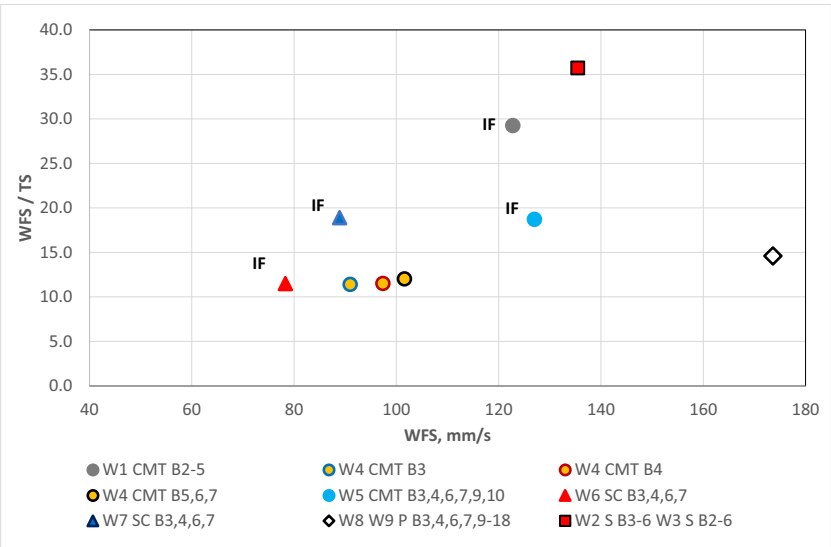

Fig. 15. Effect of WFS and WFS/TS of sidewall passes on incomplete fusion (IF) defect formation. Welds W1 through W9, processes: CMT, GMAW-SC, GMAW-P, and GMAW-S

of the FM-686 root pass in these welds resulted in unacceptably high hardness (Fig. 9b, c).

Incomplete fusion defects were experienced in the sidewall passes deposited with CMT in welds W1 and W5, and with GMAW-SC in welds W6 and W7 (Figs. 8a and 10). The poor sidewall penetration and IFDs in these welds were caused by (1) the narrow groove geometry constraining the torch weaving [16] and (2) the high surface tension of the molten pool and poor wetting characteristics of the CMT and GMAW-SC arcs [17, 18].

The CMT weld W1 utilized the same welding parameters in all fill passes in a single-pass-per-layer procedure (Fig. 6a; Table 2). The high WFS/TS ratio (Fig. 15) represented the upper range of deposition rates and heat inputs of the CMT process. However, the restricted amplitude and constant torch angle weaving pattern did not allow consistent penetration at triple points between subsequent passes and the side wall (Fig. 8a).

The CMT weld W5 and GMAW-SC welds W6 and W7 utilized lower heat input, three-bead-per-layer procedures shown in Fig. 6c, d and Tables 3 and 4. The layer central passes, B2, B5, and B8 were deposited before the sidewall passes B3, B4, B6, B7, B9, and B10, aiming to reduce dilution with the FM-686 root pass. A 5° torch angle toward the side walls was used to improve the sidewall penetration. Compared to W1, the CMT the sidewall passes through in weld W5 utilized lower deposition rates, smaller weaving amplitudes, and faster weaving frequency. However, the convex shape of central passes B2, B5, and B8 resulted in incomplete fusion among the sidewall passes and with the FM-686 root pass (Fig. 10a).

The WFS and, respectively, the deposition rate of the B2 central passes in W6, W7, and W8 were significantly reduced to limit dilution with the root pass and open wider spaces for deposition of the side passes (Figs. 12 and 13). W6 and W7 utilized the GMAW-SC process aiming to improve the sidewall penetration. The sidewall passes in W6 were run without weaving at a lower deposition rate than the CMT W5 (Tables 3 and 4; Fig. 15). This resulted in incomplete fusion defects in the sidewall passes B3 and B4 with the FM-686 root pass (Fig. 10b). The next optimization step in W7 involved extending the groove land by 5.08 mm, as shown in Fig. 1b. This allowed for weaving in the sidewall passes and increasing their deposition rate by using higher WFS and lower TS compared to W6 (Figs. 14 and 15). The incomplete fusion defects in passes B3 and B4 with the FM-686 root pass was eliminated, but some still formed in between the side wall passes (Fig. 10c).

The final optimization step in the three-pass-per-layer procedure utilized the GMAW-P process for depositing the sidewall passes in welds W8 and W9. Compared to W5, W6, and W7, passes B3, B4, B6, and B7 were deposited with significantly higher WFS and TS but with a similar deposition rate (Figs. 14 and 15). The stable droplet transfer and higher voltage GMAW-P arc, in combination with weaving in the wider weld groove, resolved the incomplete fusion problem experienced in welds W1 through W7 (Fig. 11b, c). The results of this study show that low dilution of FM-686 in the first LAS pass B2, accomplished by a low WFS/TS ratio combined with a high WFS/high TS GMAW-P process and weaving in a wider groove, is sufficient to avoid incomplete fusion defects in the sidewall passes.

4.2.3 Weld metal hardness control

The approach for reducing the weld metal hardness included utilizing a lower hardenability LAS filler metal, minimizing dilution of the FM-686 root pass in the weld metal, and introducing tempering by reheating with subsequent fill passes. ThermoClac™ simulations have shown that both LAS filler metals diluted with more than 40% FM-686 would form a fully austenitic microstructure, while 30% dilution resulted in forming about 40% martensite (Fig. 5). Reheating below the A_{C1} temperature with a subsequent fill pass would temper the martensite in underlying weld passes, while exceeding the A_{C3} would reform fresh martensite.

The welding parameters controlling the FM-686 root pass dilution in the weld metal and the bead tempering effects, in terms of WFS, TS, and WFS/TS ratio, are mapped in Figs. 15 and 16. The CMT welds W1 and W4, and GMAW-S welds W2 and W3 exhibited hardness values above 400 $HV_{0.3}$ in the first two LAS passes (Fig. 9a–c). This can be attributed to the dilution of Cr and Ni from the FM-686 root pass, resulting in the formation of a martensitic microstructure with a low A_{C1} temperature [19]. The high dilution of FM-686 in passes B2 and B3 of these welds was related to the high heat inputs and deposition rates, and low travel speeds. The reheating effects of passes B4, B5, and B6 lead to both partial tempering and hardening, resulting, respectively, from reheating below the A_{C1} and above the A_{C3} temperatures.

Efforts to reduce hardness consisted of utilizing a filler metal with a lower carbon content and increasing the number of weld passes per layer. The higher carbon content and the higher hardenability of ER100S-G filler metal (Table 1) were substituted in W4 through W9 with ER80S-G to help decrease the hardness of martensite [20]. Applying three passes per layer not only helped reduce dilution from the

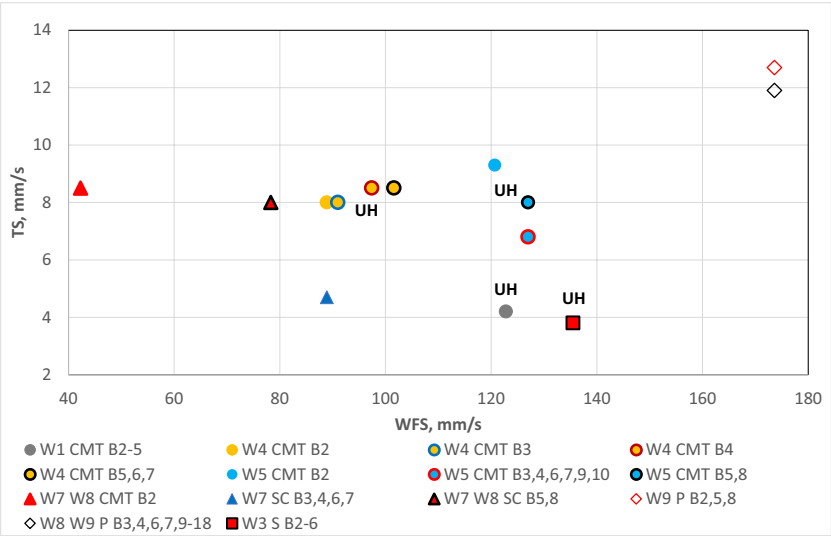

Fig. 16 Effect of WFS and TS of fill passes on weld metal hardness. UH, unacceptable high hardness. Welds W1 through W9; processes: CMT, GMAW-SC, GMAW-P, and GMAW-S

FM-686 root pass but also created a temper bead effect that reduced hardness by reheating previous weld passes below A_{C1} temperature [21–24]. Compared to the CMT W4, the reduced weaving and slightly higher deposition rate and TS in W5 reduced the hardness in pass B2 below 325 $HV_{0.3}$ (Fig. 9d). This could be attributed to the formation of mixed martensite–austenite microstructure due to the higher dilution with FM-686. The subsequent passes B3, B4, and B5 exhibited hardness up to 400 $HV_{0.3}$ due to dilution with pass B2. Passes B6 through B10 provided significant weld metal tempering.

The final optimization steps for hardness control aimed at a significant reduction of FM-686 dilution in the LAS weld metal and improving the bead tempering efficiency. The most efficient hardness reduction, in terms of minimizing the area of the ER80S-G/FM-686-diluted zone with hardness above 325 $HV_{0.3}$, was achieved in W8. The latter utilized a low WFS–low TS CMT process for pass B2 and a high WFS–high TS GMWA-P process for the sidewall tempering passes B3, B4, B6, and B7 (Figs 16 and 17). Using GMAW-SC for the sidewall passes in W7 and GMAW-P for passes B2 through B8 in W8 was less efficient in minimizing the hard diluted zone (Fig. 11). The fill passes B9 through B18 in welds W7, W8, and W9 were deposited with the GMAW-P process, resulting in the weld metal hardness in the range of 225–275 $HV_{0.3}$. Considering that lower loads in hardness testing typically provide higher hardness values, it could be expected that the undiluted passes of W7, W8, and W9 would meet the DNV 250 HV_{10} requirement for low alloy steel welds exposed to H_2S environment. The latter still needs to be confirmed with 10 kg load Vickers hardness testing. The high hardness in the highly diluted weld region is a concern for the practical application of the developed welding procedures. The effect of this hard region on the local yielding, strain accumulation, and final failure in cross-weld tensile testing was quantified using digital image correlation (DIC) in Part II of this study [25]. Its microstructure and potential susceptibility to hydrogen assisted cracking in subsea service under cathodic protection were also analyzed. Post weld heat treatment could reduce the hardness of the high dilution region.

4.3 Mechanical testing

This study is intended to demonstrate a low-alloy steel filler metal girth weld in X65 steel pipe, internally clad with Alloy 625, which satisfies the DNV with the overmatching requirement of 100 MPa for offshore reeling applications. The DNV tensile specimen design is shown in Fig. 7 aims to determine the mechanical properties in the upper portion of the weld that would experience higher tensile loads and strain levels during reeling. The minimum specified yield strength of API 5L Grade X65 steel is 450 MPa. As shown in Table 7, all three tensile test specimens from weld W7 exhibited yield strength values that significantly exceeded the DNV overmatching requirement. However, the elongation at failure was lower than the 18% DNV specification. This could be related to the fill pass hardness in W7 slightly exceeding the DNV hardness requirement and to the potential presence of weld metal pores, as shown in Fig. 11.

The elongation at failure in W7 was lower than the industry reported, 24% to 25% for undiluted ER80S-G all-weld metal [26]. This can be attributed to different gauge section designs in the DNV cross-weld specimen (Fig. 7) and in the ASTM E8/M8 all-weld metal specimen. It has to be noted that the DNV tensile specimen is inapplicable to determining the mechanical properties of the entire dissimilar FM-686/ER80S-G girth weld developed in this study. Cross-weld

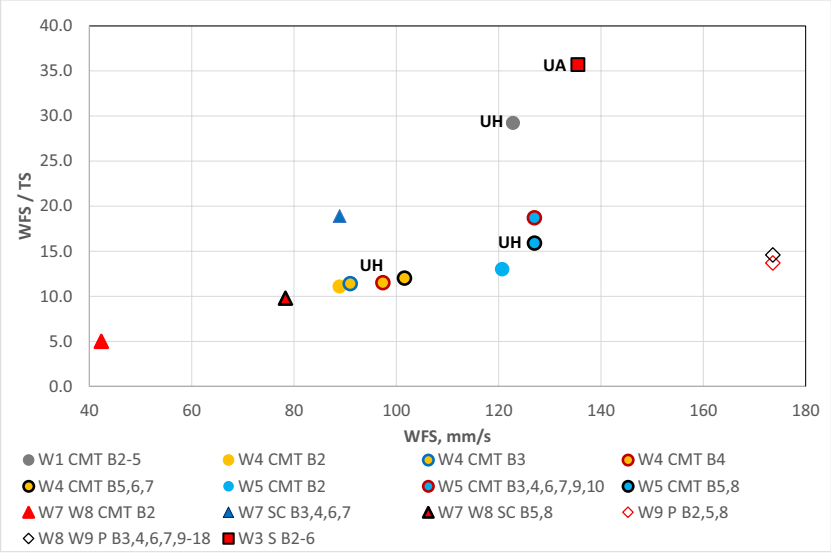

Fig. 17 Effect of WFS and WFS/TS of fill passes on weld metal hardness. UA, unacceptable high hardness. Welds W1 through W9; processes: CMT, GMAW-SC, GMAW-P, GMAW-S

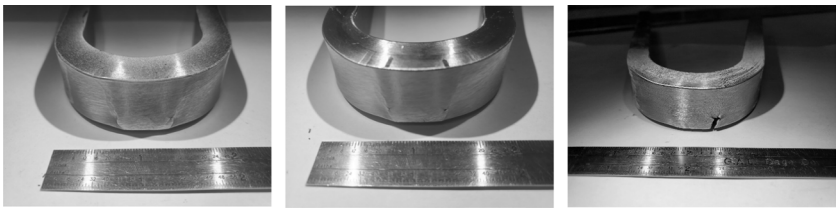

a) b) c)

Fig. 18 Bend testing results from welds 7 **a**, **b** defect-free specimens and **c** crack longer than 3 mm, originating from IFD

tensile testing of ASTM E8/M8 specimens, instrumented with digital image correlation (DIC), was performed in Part II of this study [25] to determine the mechanical properties of the entire weld metal and of separate layers in weld W8.

Two of the three specimens passed the 20% elongation bend test without cracking or disbonding (Fig. 18). This confirms the acceptable ductility of the entire weld, including the dissimilar fusion boundaries of the FM-686 root pass with the X65 steel base metal and the EG80S-G fill passes. The third sample formed a small crack from an incomplete fusion defect present before bend testing at the fusion boundary between a sidewall pass and the base metal, similar to the one shown in Fig. 10c.

5 Summary and conclusions

This study successfully demonstrated defect-free welds of higher-melting point filler metal over the root pass of a lower-melting alloy in a narrow grove configuration. It involved filler metal selection and welding procedures developed for joining API 5L Grade X65 steel pipes, internally clad with alloy 625. Optimal solutions for avoiding weld defects, weld metal hardness control, and meeting the mechanical property requirements for pipe reeling applications included:

1. Root pass of alloy 686 filler metal and fill passes of ER80S-G filler metal.
2. Low heat input–low deposition rate CMT, GMAW-SC, and GMAW-P processes.
3. Three beads per layer in the first three layers and two beads per layer in the remaining layers.
4. The central bead in the first three layers was deposited with CMT and GMAW-SC processes.
5. Side beads in the first three layers and fill beads in the remaining layers deposited with a GMAW-P process.

Using FM-686 for the root pass and depositing ER80S-G with a low-dilution three-bead per layer procedure resolved the problem of solidification cracking and the formation of shrinkage porosity experienced in welding with low alloy steel filler metals on Ni-based substrates. In comparison to dilution with FM-625, the ER80S-G weld metal diluted with FM-686 exhibited a significantly shorter solidification temperature range without the formation of the Laves phase at the terminal stage of solidification. No solidification cracking and shrinkage porosity were experienced when depositing ER80S-G using CMT and GMAW-P processes with a WFS/TS ratio below 15 at WFS between 40 and 180 mm/s.

Incomplete fusion defects in the side beads of the three-bead per layer procedure were effectively avoided by using a low deposition rate high high welding current (WFS) GMAW-P process. A defect-free weld was also produced by a two-bead per-layer CMT procedure. However, extensive dilution with the FM-686 root pass led to unacceptably high weld metal hardness.

Optimal narrowing of the high hardness region in the partially mixed ER80S-G/FM-686 weld layers was achieved by depositing the central passes in these layers with low deposition rate—low WFS CMT and GMAW-SC processes. Optimal weld metal bead tempering was provided by the low deposition rate/high WFS GMAW-P process. However, the DNV hardness requirement of $250HV_{10}$ was not met in the highly diluted weld region.

A narrow groove weld produced using the developed procedures met the yield strength and side bend requirements for reeling applications.

Acknowledgements This research was performed within the NSF Manufacturing and Materials Joining Innovation Center (Ma^2JIC) and was supported by voestalpine Bohler, Petrobras, and Vallourec Brazil.

Author contribution All authors contributed to the study's conception and design. Material preparation, data collection, and analysis were performed by Dr. Alejandro Alvarez, Dr. Boian T. Alexandrov, Dr. Martin Schmitz-Niederau, and Hermann-Josef Weber. The first draft was written by Dr. Alejandro Alvarez, and all authors commented on previous versions of the manuscript. All authors read and approved the final manuscript.

References

1. Singh MP, Arora KS, Shajan N, Pandu SR, Shome M, Kumar R, Shukla D (2019) Comparative analysis of continuous cooling transformation behavior in CGHAZ of API X-80 and X-65 line pipe steels. J Therm Anal Calorim 137(4):1155–1167
2. Azarmi F, Leither C (2012) Microstructural formation during wire arc spraying of alloy 625 on wrought alloy 625 substrate. Metall Mater Trans A 43(12):4703–4710

3. Guo B, Song S, Chacko J, Ghalambor A (2005) Offshore Pipelines. Elsevier Inc., Burlington
4. A. Det Norske Veritas, "DNV-OS-F101 Submarine Pipeline Systems," Det Norske Verita AS, 2012
5. Alexandrov BT, O'Brian E, Suma E (2023) Solidification in dissimilar metal welds of higher solidus filler metals over lower solidus substrates. In preparation
6. Yang YK, Kou S (2010) Macrosegregation mechanisms in arc welds. Sci Technol Weld Join 15(1):15–30
7. Riffel K, e Silva RHG, Carvalho L, Kejelin N (2020) An efficient alternative for joining internally clad pipes using innovative welding techniques and equipment. In: SPE Annual Technical Conference and Exhibition (Online)
8. Jones R, Nuno Pepe GB, Toguyeni G, Mair J, Schmidt T, Banse J (2013) High strength carbon steel and CRA lined pipe for reel-lay installation. In: Offshore technology conference, Houston
9. A. W. Society, AWS A5.28/A5.28M:2020 (2020) Specification for low-alloy steel electrodes and rods for gas shielded arc welding. American Welding Society, Miami
10. A. W. Society, AWS A5.14/A5.14M:2018 (2018) Specification for nickel and nickel-alloy bare welding electrodes and rods. American Welding Society, Miami
11. Alexandrov B, Hope S, Lippold J, McCracken S (2011) Weldability studies of high-Cr, Ni-base filler metals for power generation applications. Weld World 55(3-4):65–76
12. DuPont J, Robino C, Marder AR (1998) Modeling solute redistribution and microstructural development in fusion welds of Nb-bearing superalloys. Acta Mater 46(13):4781–4790
13. Alexandrov BT, Hope A, Sutton BJ, Sowards JW, Lippold J, McCracken S (2012) Susceptibility to solidification cracking in high chromium nickel-base filler metals for nuclear power application. In: Trends in welding research IX, ASM International, Chicago, pp 614–622
14. Buntain RJ, Alexandrov BT, Viswanathan G (2020) Characterization of interpass macrosegregation in narrow groove closure welds between low alloy steel pipes with alloy 625 filler metal. Mater Charact 170(110638)
15. Kuper MW, Alexandrov BT (2019) Retention of delta ferrite in the heat affected zone of grade 91 steel dissimilar metal welds. Mater Metall Trans A 50(6):2732–2747
16. Matsumura H, Nakagomi T, Takada S (2012) A study on the welding procedure of the first layer of the narrow groove welding for steel frames of buildings by welding robots. Weld Int 28(4):264–272
17. Ola O, Doern F (2014) A study of cold metal transfer clads in nickel-base INCONEL 718 superalloy. Mater Des 57:51–59
18. Phillips DH (2016) Welding engineering an introduction. John Wiley & Sons, Ltd, West Sussex
19. Kelly P, Nutting J (1960) The Martensite transformation in carbon steels, series A. Math Phys Sci 259(1296):45–58
20. Lippold JC (2015) Welding metallurgy and weldability. John Wiley & Sons, Inc, Hoboken
21. Aloraier AS, Joshi S, Price JW, Alawadhi K (2014) Hardness, microstructure, and residual stresses in low carbon steel welding with post-weld heat treatment and temper bead welding. Metall Mater Trans A 45(4):2030–2037
22. Ling K-H, Fuh Y-K, Kuo T-C, Xun-Tu S (2015) Effect of welding sequence of a multi-pass temper bead in gas-shielded flux-cored arc welding process: hardness, microstructure, and impact toughness analysis. Int J Adv Manuf Technol 81(5-8):1033–1046
23. Higuchi M, Sakamoto H, Tanioka S (1980) A study on weld repair through half bead method. IHI Eng Rev 13(2):14–19
24. Stewart J, Alexandrov B (2021) Quantification of the hardness response in the heat-affected zone of low alloy steels subjected to temper bead welding. J Manuf Process 66:325–340
25. Alvarez A, Siefert W, Alexandrov BT (2023) Low alloy steel girth welds in X65 steel pipes internally clad with alloy 625. Part II. In: Microstructure and local mechanical properties. under preparation for submission to welding in the world
26. Voestalpine, "Bohler Welding," Voestalpine, [Online]. Available: http://www.bohlerwelding.com. Accessed 13 Apr 2021